

## RESEARCH ARTICLE

10.1002/2015JB012358

## Key Points:

- First case study of assessing VHR stereo imagery to determine height changes in an earthquake
- Elevations from tristereo have slightly (~15%) smaller uncertainties than bistereo
- Coseismic height changes mapped using the Pleiades DEM are comparable to differential lidar

## Correspondence to:

Y. Zhou,  
yu.zhou@earth.ox.ac.uk

## Citation:

Zhou, Y., B. Parsons, J. R. Elliott, I. Barisin, and R. T. Walker (2015), Assessing the ability of Pleiades stereo imagery to determine height changes in earthquakes: A case study for the El Mayor-Cucapah epicentral area, *J. Geophys. Res. Solid Earth*, 120, 8793–8808, doi:10.1002/2015JB012358.

Received 13 JUL 2015

Accepted 3 DEC 2015

Accepted article online 13 DEC 2015

Published online 28 DEC 2015

# Assessing the ability of Pleiades stereo imagery to determine height changes in earthquakes: A case study for the El Mayor-Cucapah epicentral area

Yu Zhou<sup>1</sup>, Barry Parsons<sup>1</sup>, John R Elliott<sup>1</sup>, Ivana Barisin<sup>1</sup>, and Richard T Walker<sup>1</sup>
<sup>1</sup>COMET, Department of Earth Sciences, University of Oxford, Oxford, UK

**Abstract** High-resolution surface topography is valuable for studying coseismic fault zone deformation and fault geometry. It enables us to measure three-dimensional surface displacements in earthquakes, as shown in recent studies that used light detection and ranging (lidar) to determine coseismic motion. However, the applicability of lidar is limited by its relatively high cost and low availability. In this study, we use the 2010 El Mayor-Cucapah earthquake to demonstrate the capability of Pleiades stereo imagery to measure coseismic vertical ground displacement. We acquired post-earthquake Pleiades tristereo imagery from backward, near-nadir, and forward orientations for a 45 km × 7 km portion of the epicentral area. One meter resolution digital elevation models (DEMs) were produced with the four different combinations of incidence angles and compared to the post-earthquake lidar DEM. Elevations from tristereo have slightly (~15%) smaller uncertainties than bistereo as the tristereo DEM incorporates more observations. Elevation differences between the Pleiades and post-earthquake lidar DEMs show that the vertical accuracy of the Pleiades DEMs is ~0.3 m. By differencing the Pleiades DEM and the pre-earthquake, 5 m resolution lidar DEM, we mapped meter and submeter offsets along the faults obtaining results comparable to a previous study that differenced the two lidar DEMs. This is the first case study of assessing very high resolution (VHR) satellite stereo imagery to determine submeter vertical ground displacement in an earthquake. By extension, we expect it to be possible to measure submeter vertical offsets occurring in earthquakes using pre-earthquake and post-earthquake VHR stereo imagery.

## 1. Introduction

Late Quaternary fault activity is recorded in the landscape in the form of fault scarps [Wallace, 1977; Hanks et al., 1984; Avouac and Peltzer, 1993; Oskin et al., 2007] and displacements of landforms such as river channels and terraces [Ritz et al., 1995; Wesnousky et al., 1999; Cowgill, 2007]; these pieces of evidence provide important information about past earthquakes and potentially characterize future seismic events that are likely to occur [Gold and Cowgill, 2011; Oskin et al., 2012]. Until relatively recently, such evidence could only be investigated in the field, but the short spatial scale field observations may have limited our understanding of fault behavior in continental regions and therefore the estimation of the associated seismic hazard [Jackson, 2001; England and Jackson, 2011; Oskin et al., 2012; Zhang, 2013]. In the last few decades remote sensing has emerged as a powerful tool for studying active faulting over large scales. Satellite imagery (e.g., Landsat, Advanced Spaceborne Thermal Emission and Reflection, and SPOT) has been used to identify fault geometries, surface ruptures, and offsets in recent and ancient earthquakes [e.g., Molnar and Tapponnier, 1975; Fialko et al., 2001; Dominguez et al., 2003; Klinger et al., 2005; Avouac et al., 2006; Campbell et al., 2015].

Matching of pre-earthquake and post-earthquake optical and radar imagery of the epicentral region has the potential to measure horizontal surface displacements at subpixel accuracy [Leprince et al., 2007] and is often used to investigate coseismic deformation [e.g., Fialko et al., 2001; Michel and Avouac, 2002; Binet and Bollinger, 2005; Avouac et al., 2014]. However, these approaches cannot measure height changes directly. Light detection and ranging (lidar) surveys have been a valuable tool for determining vertical offsets in earthquakes [Oskin et al., 2012; Elliott et al., 2012; Ren et al., 2015], but its relatively high cost and low availability have limited its applicability, particularly as pre-earthquake lidar acquisitions are rare [Nissen et al., 2014].

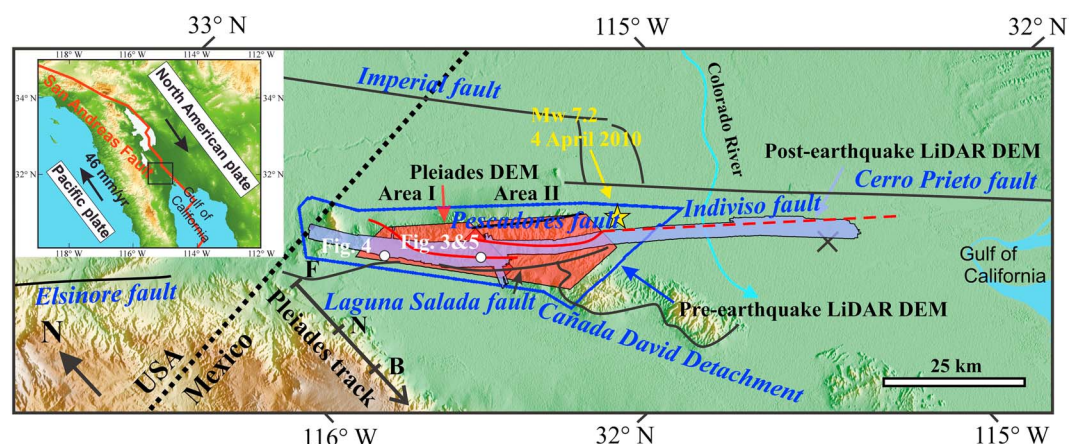


**Figure 1.** Tectonic setting of the El Mayor-Cucapah earthquake rupture. The 2010 El Mayor-Cucapah earthquake occurred on a complex, multisegment fault system which forms the right-lateral transform boundary of the Pacific and North America plates in Southern California. The earthquake initiated on the Indiviso fault (yellow star) and ruptured bilaterally. Two sets of Pleiades tristereo imagery were acquired in this study (marked as Areas I and II by filled red polygon). These two sets of Pleiades imagery overlap at the northwestern end of the Pescadores fault (the dark red area). Forward (F)/nadir (N)/backward (B) orientations are marked on the Pleiades track. Pre-earthquake and post-earthquake lidar DEMs (downloaded from <http://www.opentopography.org/>) are marked by blue outline and filled purple polygons. White dots indicate the areas in Figures 3–5. Faults from Fletcher *et al.* [2014] are marked by red (the 2010 rupture) and black lines.

New generations of very high resolution (VHR) satellites, e.g., Pleiades 1A/1B (0.7 m panchromatic), GeoEye-1 (0.41 m panchromatic), WorldView-1/2 (0.46 m panchromatic), and WorldView-3 (0.31 m panchromatic), allow rapid 3-D reconstruction due to their short revisit time and stereo capability [de Lussy *et al.*, 2005; Fraser and Ravanbakhsh, 2009; Mitchell and MacNabb, 2010; Poli and Toutin, 2012; Bernard *et al.*, 2012]. VHR stereo imagery can in principle measure surface topography with decimetric precision, comparable to lidar surveys, but at a much lower cost and with higher availability. Recent studies have evaluated the ability of VHR imagery to trace horizontal displacements [Barnhart *et al.*, 2011; Stumpf *et al.*, 2014] and Pleiades stereo imagery to map meter-scale elevation changes of glaciers [Berthier *et al.*, 2014]. It is an open question as to how well 3-D mapping based on VHR stereo imagery captures submeter height changes occurring in an earthquake in order to characterize 3-D surface slip [Zhou *et al.*, 2015] and fault geometry. The aim of this study is to assess the capability of the Pleiades satellites to determine such height changes.

The 2010  $M_w$  7.2 El Mayor-Cucapah earthquake [Wei *et al.*, 2011; Oskin *et al.*, 2012] is chosen as a case study because it is the first time that an earthquake rupture has been completely captured by differential lidar [Oskin *et al.*, 2012]. We explore whether the Pleiades stereo imagery also has the ability to capture the vertical ground displacement resulting from the earthquake at a decimetric level of accuracy. In addition, because the Pleiades satellite system is capable of acquiring three along-track images of the same area in a single pass (i.e., the tristereo mode) due to its steerable platform, we want to compare the quality of DEM generation from tristereo and bistereo modes, in order to compare their relative abilities to accurately capture height changes in earthquakes.

Therefore, we requested acquisitions of Pleiades tristereo imagery for a 45 km  $\times$  7 km portion of the epicentral area of the El Mayor-Cucapah earthquake to coincide with the post-earthquake lidar DEM (Figure 1). We first produce 1 m resolution digital elevation models (DEMs) with the three combinations of bistereo images and the single tristereo mode. The uncertainties in the Pleiades DEMs are estimated using the post-earthquake lidar DEM assuming this is the most accurate. By differencing the Pleiades and pre-earthquake lidar DEMs, we map the surface deformation occurring in the earthquake and then compare our result to the previous study that differenced the two lidar DEMs [Oskin *et al.*, 2012]. Using the near-field surface deformation, we are also able to examine the fault geometry.

## 2. Overview of the 2010 El Mayor-Cucapah Earthquake

The 4 April 2010 El Mayor-Cucapah earthquake (Mexico) occurred on a complex, multisegment fault system that forms part of the right-lateral transform boundary of the Pacific and North America plates in Southern

California (Figure 1) [Hauksson *et al.*, 2011]. Geological and geodetic studies indicate that more than ~90% of the plate motion (~46 mm/yr) in the vicinity of the 2010 rupture is accommodated on the Laguna Salada, Cañada David, Cerro Prieto, and Imperial fault systems [Bennett *et al.*, 1996; Fletcher *et al.*, 2014]. However, the 2010 earthquake did not rupture any of these four, well-known faults [Fletcher *et al.*, 2014]. Instead, the highly segmented rupture occurred on a series of obscure and, in part, previously unidentified faults (such as the Indiviso fault that is covered by thick sediments). Geodetic and seismological observations indicate that the rupture initiated with a normal faulting subevent on the Indiviso fault and propagated bilaterally northward and southward with predominantly strike-slip motion [Wei *et al.*, 2011]. The average right-lateral surface slip over the 120 km rupture length was 2 m [Wei *et al.*, 2011].

A low-resolution lidar survey (with a point density of 0.02 points/m<sup>2</sup>) was undertaken from 31 July to 7 August 2006 by the Instituto Nacional de Estadística y Geografía (INEGI) of Mexico, and 4 months after the earthquake in August 2010, high-resolution lidar data (with a point density of 9.12 points/m<sup>2</sup>) were collected along the fault rupture by the National Center for Airborne Laser Mapping (NCALM) [Oskin *et al.*, 2012; Glennie *et al.*, 2014]. The relative height accuracy of the post-earthquake lidar data is estimated to be 4–9 cm by comparing the elevation differences within areas of swath overlap [Oskin *et al.*, 2012]. Elevation changes from differencing the two lidar DEMs reveal large distributed deformation over the structurally complex Sierra Cucapah area [Oskin *et al.*, 2012; Glennie *et al.*, 2014]. The pre-earthquake lidar DEM was reprocessed by Glennie *et al.* [2014]. Both the corrected pre-earthquake and post-earthquake lidar DEMs are freely available from <http://www.opentopography.org/>. In addition to the image-based studies of this earthquake, Fletcher *et al.* [2014] and Teran *et al.* [2015] investigated the surface rupture and fault structure in the field.

### 3. Data and Methods

#### 3.1. Data Sets

The Pleiades satellite constellation consists of two identical satellites launched on 17 December 2011 (Pleiades 1A) and 2 December 2012 (Pleiades 1B), in Sun-synchronous orbits (98.2° inclination) offset 180° from each other, which provide VHR optical images worldwide with a revisit interval of 24 h due to steering ability of platform [de Lussy *et al.*, 2006, 2012]. Panchromatic images are acquired with a 70 cm nadir resolution and delivered with a nominal resolution of 50 cm [de Lussy *et al.*, 2012] over a swath footprint of 20 km. Multispectral images are acquired simultaneously and delivered with a nominal resolution of 2 m. The Pleiades satellite system is capable of acquiring three images of the same area in a single pass with B/H ratios (baseline/height, height ≈ 694 km) of 0.1 to 0.5 with the tristereo mode, i.e., ~70–350 km separation and corresponding stereo angles of ~6–28° [de Lussy *et al.*, 2006]. In this study, tristereo data were acquired by Pleiades 1B over a 45 km × 7 km area on 17 March 2014 (Figure 1). Images are acquired with a 20 km footprint, so the region was tasked in two areas. The along-track incidence angles of the forward (F)/near-nadir (N)/backward (B) orientations for the NW and SE data sets are –13.4°/–1.2°/11.3° (I) and –9°/3.6°/15.8° (II), respectively.

#### 3.2. DEM Generation

The tristereo data were processed using the Leica Photogrammetry Suite. The initial task was to define the geometric model. In remote sensing systems, a geometric model is used to describe the relationship between image (*x*, *y*) and ground (*X*, *Y*, *Z*) coordinate systems. For traditional frame cameras, the geometric model can be represented with a standard pinhole model [Gremban *et al.*, 1988], and the derivation is relatively simple. However, for pushbroom imaging systems (such as the Pleiades satellites), although each scanning line could be represented rigorously with the pinhole model, such a model would be rather complex as each line needs to be treated as an individual pinhole model with different attitude parameters. Therefore, a single set of rational polynomial functions (RPFs) is introduced to approximate all of these rigorous sensor models [Hu *et al.*, 2004; Fraser and Hanley, 2005]. The RPFs take the following form:

$$x = \frac{P_1(X, Y, Z)}{P_2(X, Y, Z)} \quad (1)$$

$$y = \frac{P_3(X, Y, Z)}{P_4(X, Y, Z)} \quad (2)$$

where  $P_i$  ( $i = 1, 2, 3, 4$ ) is a third-order polynomial function. The coefficients of these polynomial functions are given as 80 rational polynomial coefficients (RPCs) (20 coefficients for each polynomial function). However, the RPC model does not have any physical meaning and does not adequately take account of the true spatial

orientation of each scan line and the attitude, position, and velocity of the sensor [Fraser and Hanley, 2005]. The sensor errors can be modeled as biases in image coordinates—shifts to compensate for small attitude errors and drift or an affine (linear function) distortion to compensate for time-dependent errors [Fraser and Hanley, 2005].

To compensate for such shift and drift terms, equations (1) and (2) can be rewritten as

$$x + a_1 + a_2 \cdot x + a_3 \cdot y = \frac{P_1(X, Y, Z)}{P_2(X, Y, Z)} \quad (3)$$

$$y + b_1 + b_2 \cdot x + b_3 \cdot y = \frac{P_3(X, Y, Z)}{P_4(X, Y, Z)} \quad (4)$$

where  $a_i$  and  $b_i$  ( $i = 1, 2, 3$ ) describe an affine transformation to correct for the errors in sensor orientation.

Given that in our case we had no ground control points (GCPs), we identified more than 40 tie points, evenly distributed over the imagery, to calculate both the shift parameters  $a_i$  and  $b_i$  and the ground coordinates of each tie point simultaneously (i.e., bundle adjustment) [Groddecki and Dial, 2003]; the residual errors of the tie points are less than 0.2 pixels. After applying the simple shift corrections to the RPC model, a pixel-by-pixel matching procedure based on a least squares adjustment was implemented with a relatively small window size of 5×5 pixels to avoid strong smoothing of the topographic surface [Stumpf et al., 2014]. We used 0.3 as the minimum correlation coefficient for matching. A lower correlation coefficient threshold generates more matching points, but the matching is less reliable. The correspondence (i.e., two points in different images ( $x_1, y_1$ ) and ( $x_2, y_2$ ) corresponding to the same point ( $X, Y, Z$ ) on the ground) from pairwise matching was used to estimate the ground coordinates via equations (3) and (4). The resulting point cloud ( $X, Y, Z$ ) was filtered by averaging within a cell of 1 m and then gridded with a pixel spacing of 1 m (World Geodetic System 84 universal transverse Mercator 11N) using continuous curvature splines in tension with a tension factor of 0.75 [Smith and Wessel, 1990]. The spline interpolation yields a root-mean-square (RMS) error of ~0.3 m. Following the same procedure, point clouds and DEMs have been produced with four different combinations of incidence angles (B-N, N-F, B-F, and B-N-F).

## 4. Evaluation of the Pleiades DEMs

### 4.1. Point Clouds

The density of a point cloud determines the ground resolution of the raster DEM. To evaluate the ground resolution of the Pleiades DEMs, we calculated the densities of the point clouds. The raw point cloud has the lowest average point density of ~0.7 points/m<sup>2</sup> for B-F, ~1.0 point/m<sup>2</sup> for B-N and N-F, and the greatest average density of ~3.0 points/m<sup>2</sup> for tristereo (B-N-F). However, given that the points are unevenly distributed due to vegetation and topography, average point density may be an inadequate measure for evaluating the ground resolution of the DEMs. Therefore, we examined the number of points within a grid cell of 1 m (the statistics are shown in Figure 2). Approximately 47% of the point cloud from B-N and N-F has a point density of ≥1 point/m<sup>2</sup>, while ~35% of the point cloud from B-F reaches this resolution. For tristereo, ~65% of the point cloud has a point density of ≥1 point/m<sup>2</sup>. The point densities of the various point clouds suggest that tristereo improves the spatial resolution of the DEMs by 50% compared to bistereo (Figure 3 shows an example of the advantage of incorporating images from three viewing angles). The wide stereo angle (B-F) makes matching difficult and generates a very sparse point cloud especially over the mountainous areas. B-N and N-F work well for the majority of the area, but each is affected by topographic shadowing in different ways. Tristereo makes full use of all three viewing angles and provides a very dense point cloud. However, ~5% of the imagery is covered by mostly featureless areas, e.g., shadows or desert salt flats (Figure 4), where the point density is lower than 0.04 points/m<sup>2</sup>, even for the tristereo.

### 4.2. Accuracy of the Pleiades DEMs

The accuracy of the Pleiades DEMs is evaluated through a comparison with the post-earthquake lidar DEM. Due to errors in the sensor models, the absolute location accuracy of Pleiades 1A and 1B based on the RPFs only is reported to be 8.5 m and 3.5 m, respectively [Oh and Lee, 2014]. This location error will result in large elevation differences between the two DEMs. As shown in Figure 5a, elevation differences between the non-coregistered Pleiades and lidar DEMs are strongly correlated with the slope-facing direction. Therefore, before



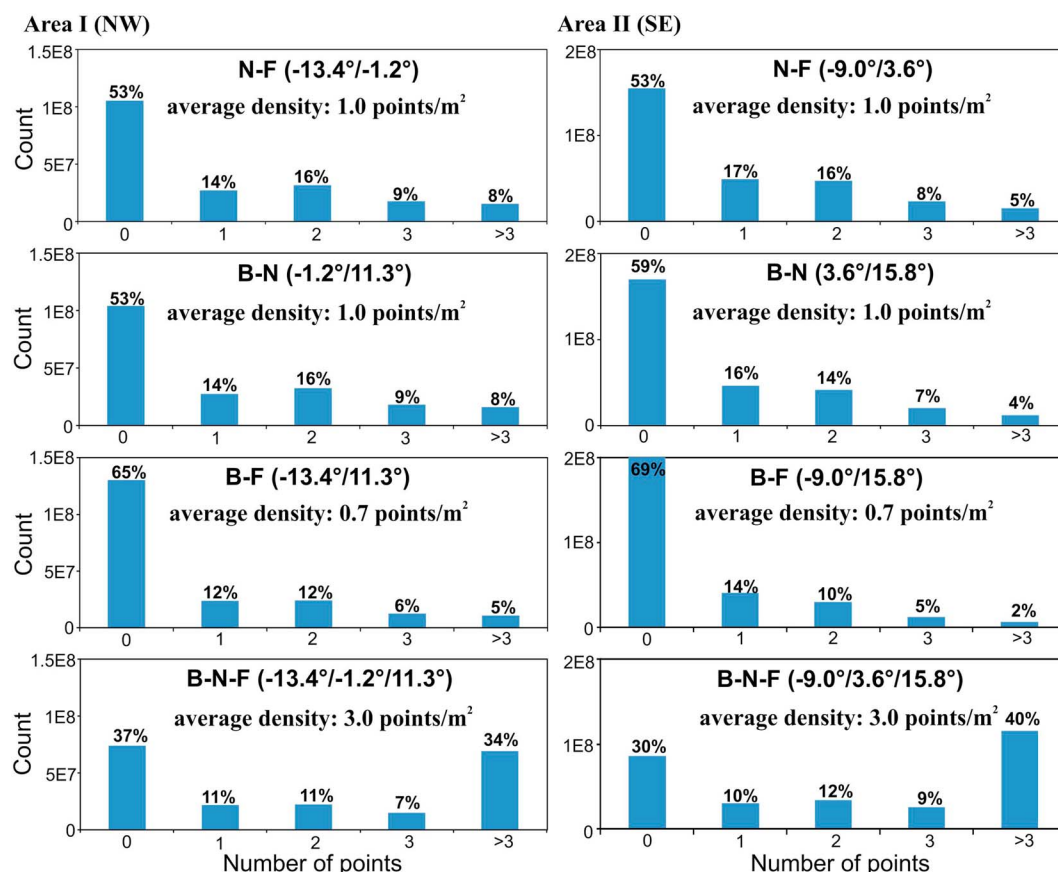


**Figure 2.** Statistics of the number of points within a grid cell for a grid spacing of 1 m for B-N, N-F, B-F, and B-N-F combinations for the two tristereo data sets (Areas I and II, see Figure 1). If the number of points is greater than or equal to 1, the cell has at least 1 measurement and therefore can be gridded with a spacing of 1 m. For tristereo, ~65% of the DEM can reach a spatial resolution of 1 m.

comparing the Pleiades and lidar DEMs, they need to be coregistered. Different image matching algorithms including cross-correlation [Leprince *et al.*, 2007] and iterative closest point (ICP) [Besl and McKay, 1992; Nissen *et al.*, 2012] can reduce the misregistration between the two DEMs. We ran ICP with a square window of 100 m, 200 m, and 500 m and compared the results with those from the cross-correlation and ICP methods using the whole imagery. Figure 5 shows the elevation differences after coregistration with different methods have been largely reduced but still increase with surface slope. This observation suggests that there is a residual coregistration error of ~0.5 m that cannot be removed by either a simple shift in *x* and *y* directions or a rigid body transformation, as the positioning error is a function of surface topography. The cross-correlation result is similar to the results from the ICP method. We prefer the cross-correlation method as the ICP algorithm is very computationally intensive. Moreover, ICP may distort the geometry of the Pleiades DEM. Our test on ICP with a window size of 100 m shows a much larger rotation (an order of magnitude or more) than those with a window size of 200 m and 500 m; such distortion results in the larger elevation difference after coregistration (Figure 5e). Small windows of <200 m are therefore not recommended.

After transforming the Pleiades DEMs to the lidar coordinate system, we differenced the Pleiades and post-earthquake lidar DEMs. When compared to the post-earthquake lidar DEM, the Pleiades DEMs have a mean elevation difference of 1 m to 4 m, with a standard deviation of 0.5 m to 0.7 m (Figure 6). Fortunately, the mean difference, caused by a lack of GCPs for absolute calibration of the Pleiades DEMs, is not an issue in terms of determining relative height changes in earthquakes. The tristereo DEM has a smaller uncertainty (0.53–0.62 m) than the bistereo DEMs (0.55–0.71 m). Figure 7 shows that the elevation difference between the DEMs increases with surface slope due to topography-related misregistration. With topographic slopes of less than 10°, the standard deviation of the elevation difference is 0.30 m; this is mainly caused by the

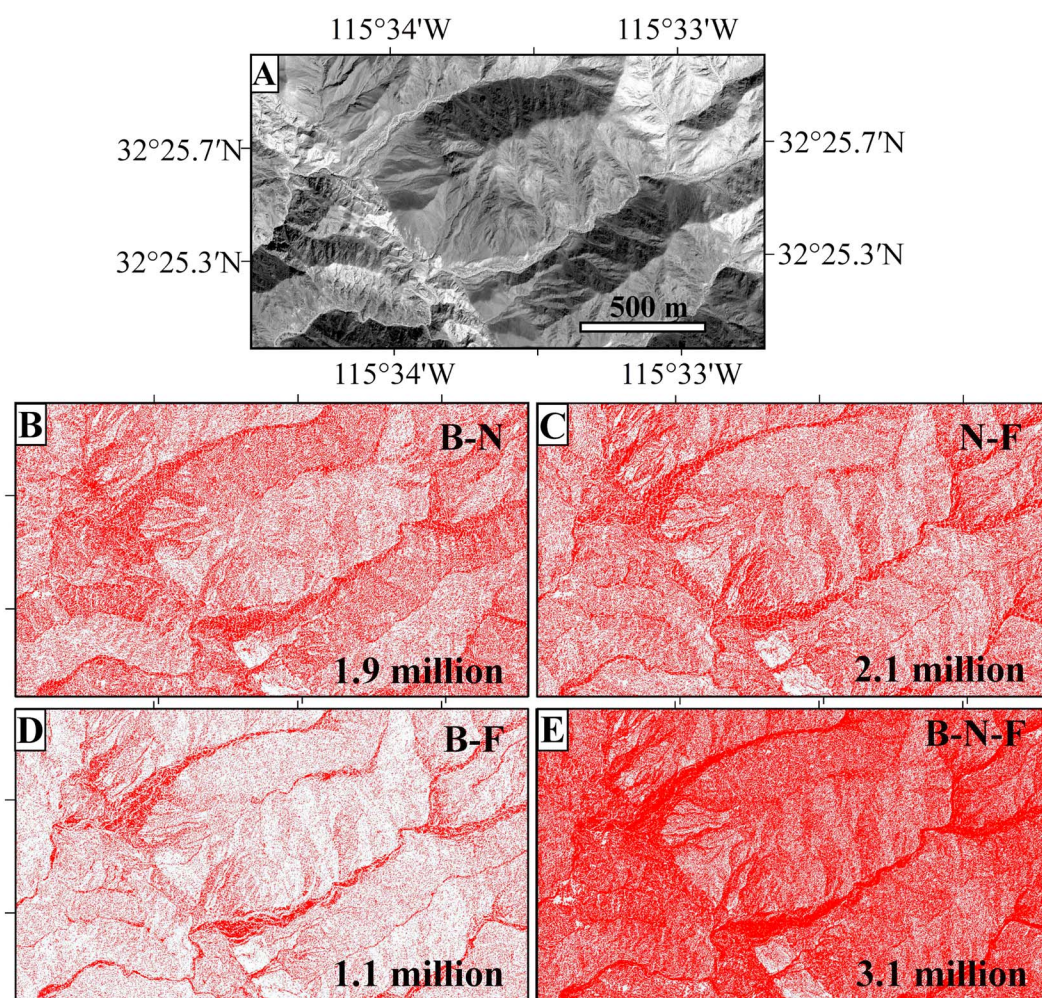


**Figure 3.** Point clouds generated from Pleiades stereo imagery (see Figure 1 for location). (a) An orthorectified image (covering an area of  $\sim 4.5$  million  $\text{m}^2$ ). Red dots are the gridded matching points from (b) B-N (1.9 million), (c) N-F (2.1 million), (d) B-F (1.1 million), and (e) tristereo (3.1 million). Each dot indicates at least 1 point within a grid of 1 m.

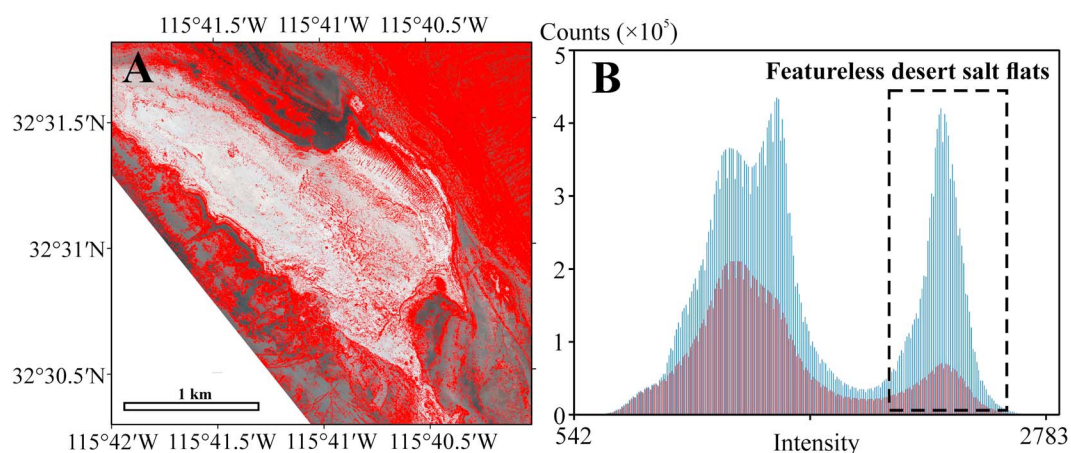


**Figure 4.** (a) An example of mostly featureless desert salt flats with few matching points (red points) from tristereo data with image below (see Figure 1 for location). (b) Histogram of the image is shown in blue. Histogram in red shows the areas where matching points have been found. In most areas, over 50% of the pixels can be matched, whereas in mostly featureless desert salt flats (bright area in Figure 4a), only 20% of the pixels were matched.



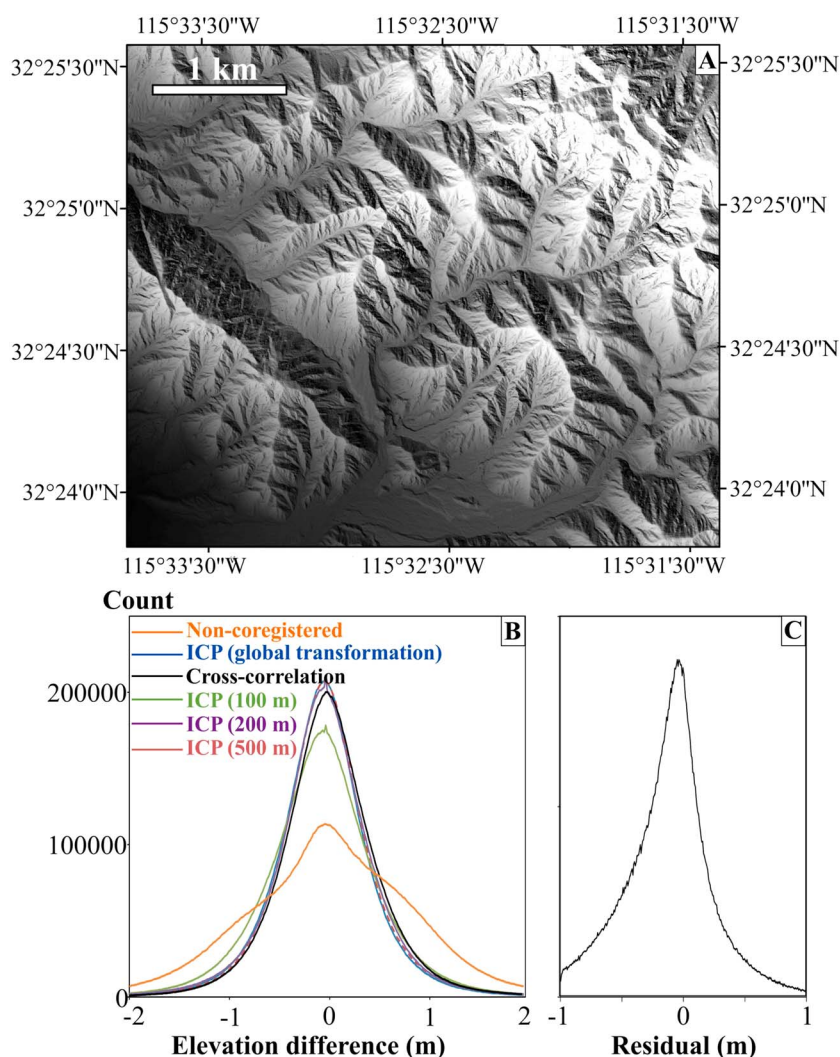


**Figure 5.** Coregistration of the Pleiades tristereo and post-earthquake lidar DEMs (see Figure 1 for location). (a) Shaded-relief Pleiades tristereo DEM. (b) Histograms of the elevation differences. (c) Histogram of the interpolation error in gridding with a pixel spacing of 1 m using continuous curvature splines in tension with a tension factor of 0.75. The spline interpolation has an RMS error of  $\sim 0.3$  m. (d) Elevation difference map between the noncoregistered DEMs. Elevation difference maps after coregistration using (e) cross-correlation (translation in  $X$  and  $Y$  directions), (f) ICP (a single transformation for the image, three translations, three rotations, and one scaling parameter), (j) ICP with a window size of 100 m, (k) ICP with a window size of 200 m, and (l) ICP with a window size of 500 m. (g–i) and (m–o) Elevation differences as a function of surface slope.

elevation errors in the Pleiades DEM. For topographic slopes of  $30^\circ$ – $50^\circ$ , the standard deviation is 0.56 m for tristereo, resulting from a combination of the elevation error in the Pleiades DEM and the residual misregistration error between the lidar and Pleiades systems. The DEMs from B-F and tristereo show a very good agreement in flat areas although the point cloud from B-F is very sparse; this suggests that the wide stereo angle provides a good geometric accuracy. With steep slopes, the standard deviation of the DEM from B-F becomes much larger, because the sparse point cloud cannot represent the rough topography well. Therefore, for mountainous areas, a wide stereo angle of  $\sim 25^\circ$  is not as suitable. To avoid the contamination of the residual misregistration error, we evaluate the vertical accuracy of the Pleiades DEMs within areas with slopes of less than  $10^\circ$  only. The two DEMs are independent measurements, and the post-earthquake lidar DEM was suggested to have a vertical uncertainty of less than 0.1 m [Oskin *et al.*, 2012]; therefore, the relative vertical accuracy of the Pleiades DEMs is  $\sim 0.3$  m. It should be noted that over a large spatial scale ( $\geq 20$  km), it may be difficult to capture this level of height change since GCPs would be needed for coregistration.

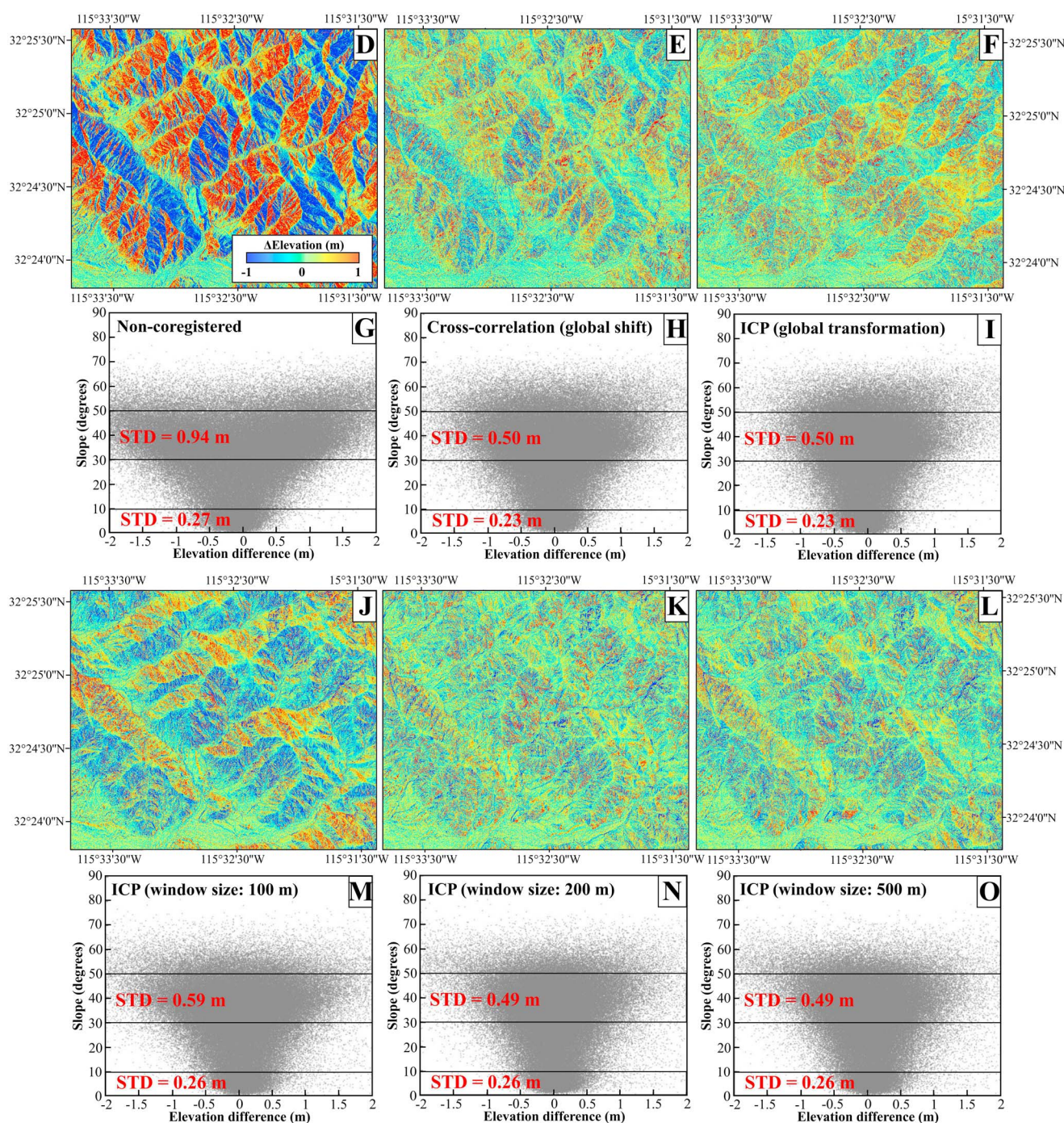
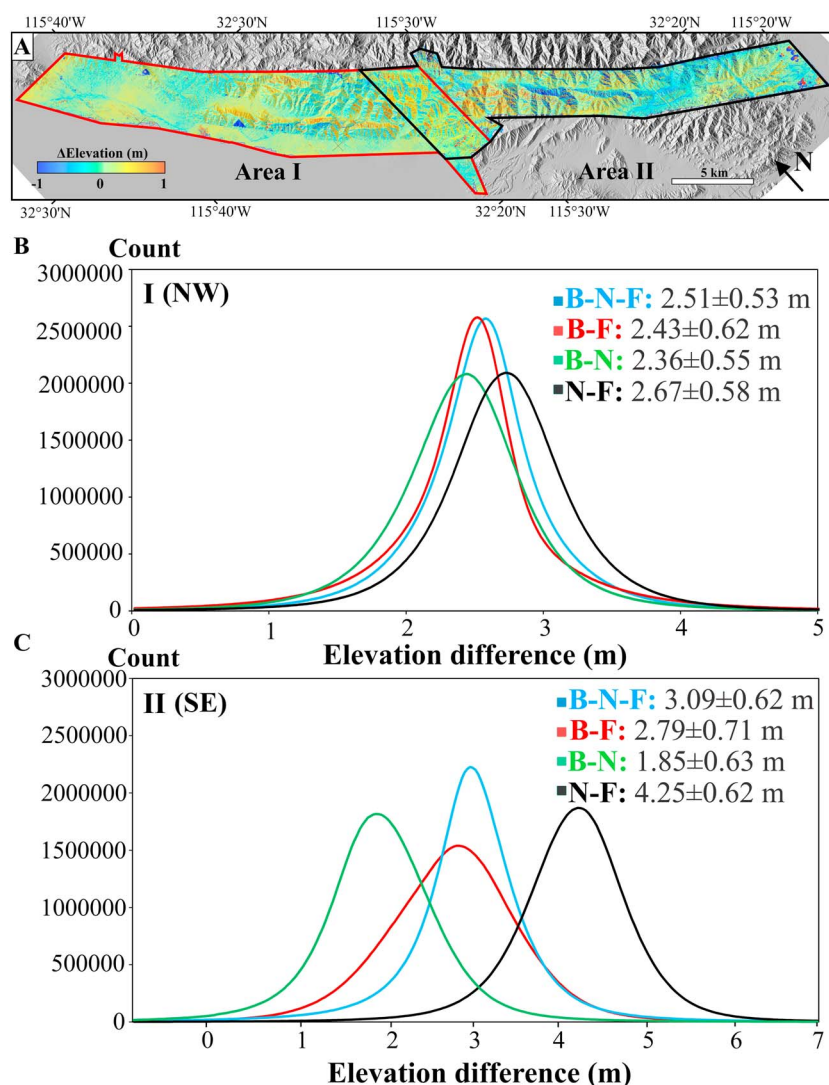


Figure 5. (continued)

## 5. Surface Deformation Using the Pleiades DEM and Discussion of Fault Geometry

Our analysis of the accuracy of the Pleiades DEM shows that it is capable of capturing submeter height changes over a length scale of  $\leq 20$  km. To estimate the height changes occurring in the earthquake, we differenced the Pleiades and pre-earthquake lidar DEMs. As there is an average of 2 m right-lateral surface slip, direct differencing without accounting for such lateral slip will yield biased measurements of height changes. In order to show the biases and make a direct comparison with the result from *Oskin et al.* [2012], we first differenced the two DEMs without correcting for the lateral slip. In the following section, we calculate the horizontal displacements and correct for these displacements before differencing the two DEMs.





**Figure 6.** (a) Elevation difference map between the tristereo Pleiades and post-earthquake lidar DEMs. (b) and (c) Histograms of the elevation difference between the Pleiades (Areas I and II marked in red and black polygons in Figure 6a) and post-earthquake lidar DEMs. Compared to the post-earthquake lidar DEM, the Pleiades DEMs have a mean elevation difference of 1 m to 4 m, with a standard deviation of 0.5 m to 0.7 m. Tristereo has a slightly smaller uncertainty (0.53–0.62 m) than bistereo (0.55–0.71 m). The mean elevation difference is due to a lack of ground control points for absolute calibration.

### 5.1. Biased Measurements of Height Changes

For a direct comparison with the study by *Oskin et al.* [2012], we first differenced the 1 m tristereo Pleiades DEM and the pre-earthquake, lower resolution (5 m) lidar DEM without accounting for the horizontal displacement. The pre-earthquake lidar DEM that we used in the study has been reprocessed by *Glennie et al.* [2014] by removing the majority of systematic errors due to the mirror/laser beam misalignment. The elevation difference map (Figures 8a and 8b) shows meter and submeter offsets along the faults, directly comparable to the result obtained by differencing the two lidar DEMs [*Oskin et al.*, 2012]. For example, profile X-X' (Figure 8d) shows a vertical displacement of 1.1 m across the Paso Inferior Accommodation Zone and an offset of 0.6 m across the Borrego fault, in good agreement with the previous study by *Oskin et al.* [2012] (Figure 8c); the profile also shows a  $\sim 0.2$  m vertical displacement across the Laguna Salada fault. When differencing the post-earthquake lidar and Pleiades DEMs, we got a difference of 0.3 m, consistent with the errors in flat areas in Figure 7. We also differenced the bistereo Pleiades DEMs and the pre-earthquake lidar DEM and obtained very similar results. The level of consistency found between offsets measured in our study using the Pleiades DEM and the previous study using the lidar DEM [*Oskin et al.*, 2012] demonstrates the capability of the Pleiades

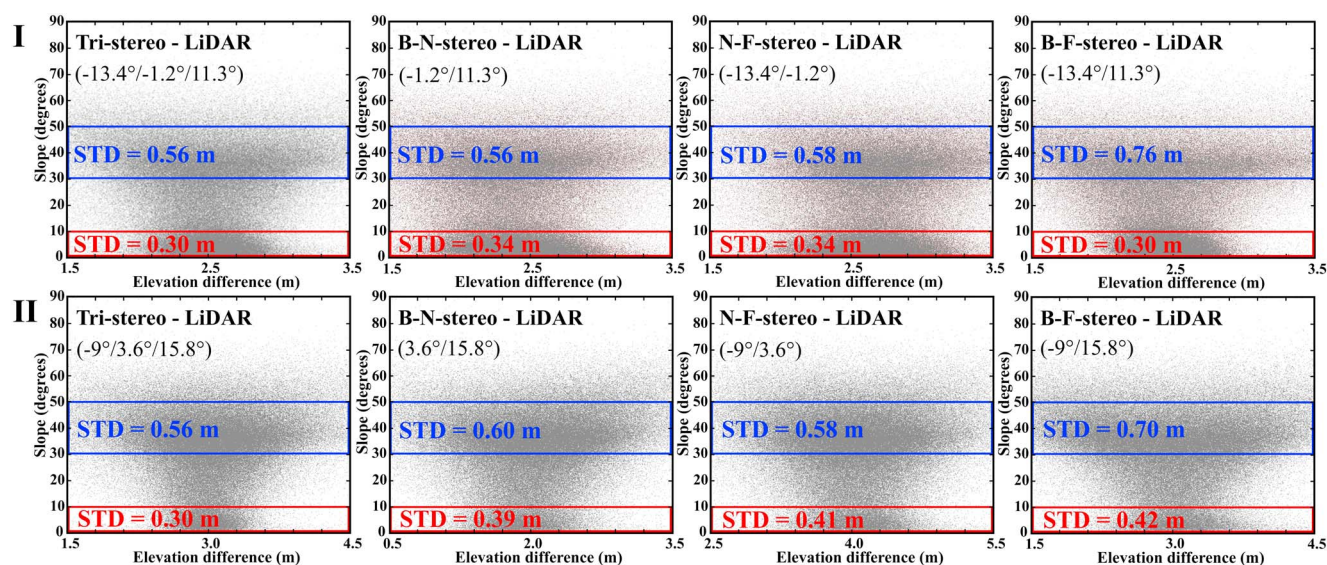


**Figure 7.** The elevation difference between the Pleiades and lidar DEMs increases with ground slope. For topographic slopes of less than  $10^\circ$ , the standard deviation of the elevation difference is  $\sim 0.30$ – $0.40$  m for all four combinations; for topographic slopes of  $30^\circ$ – $50^\circ$ , the standard deviation is  $\sim 0.56$  m for B-N, N-F, and tristereo.

DEM in measuring submeter vertical offsets with decimetric relative accuracy. *Oskin et al.* [2012] focused on the Paso Inferior Accommodation Zone where topographic slopes are less than  $3^\circ$ . Away from flat areas, the height changes are biased and strongly correlated with surface slope due to the large right-lateral coseismic slip (Figure 8a).

## 5.2. Correcting for Horizontal Displacement

To estimate unbiased height changes, we need to account for the right-lateral slip in the earthquake. We first estimated the horizontal displacements from the Pleiades and pre-earthquake lidar DEMs using the COSI-Corr software package (freely available from [www.tectonics.caltech.edu/slip\\_history/spot\\_coseis/index.html](http://www.tectonics.caltech.edu/slip_history/spot_coseis/index.html)), which measures horizontal surface displacements with an accuracy of  $\sim 1/10$  of the input pixel size [Leprince et al., 2007; Hollingsworth et al., 2012; Ayoub et al., 2009]. The Pleiades DEM was downsampled to 5 m to match the pre-earthquake lidar DEM. The subpixel matching procedure estimates horizontal displacements by cross-correlating the pre-earthquake and post-earthquake DEMs in small windows. The cross correlation is implemented in the frequency domain and the displacement retrieved from the phase difference of their Fourier transform [Leprince et al., 2007; Ayoub et al., 2009]. We used a correlation window of 64 pixels as a first step, followed by 32 pixels, with a step of 4 pixels (20 m). The resulting east-west and north-south components of the horizontal displacement were filtered using the nonlocal means algorithm (Figures 9a and 9b) [Ayoub et al., 2009]. Although Glennie et al. [2014] had corrected for processing errors in the pre-earthquake lidar DEM and such corrections can remove the artifacts in the east-west displacement (Figure 9a), the north-south displacement (Figure 9b) still shows large systematic deviations, resulting from the remaining errors in the laser beam alignment in the pre-earthquake lidar DEM. When differencing the Pleiades and pre-earthquake lidar DEMs, we also need to account for these laser beam alignment errors as well as the horizontal motion. It would be possible to correct for the horizontal motion using the pre-earthquake and post-earthquake SPOT-5 images [Barišin et al., 2015], but we would then need to do an additional correction to take account of the alignment errors in the pre-earthquake lidar DEM. It is therefore simplest to apply both corrections at once using the horizontal displacements shown in Figures 9a and 9b to the Pleiades DEM and then difference the corrected Pleiades and pre-earthquake lidar DEMs to obtain unbiased measurements of height changes.

Compared to the biased elevation difference, the resulting elevation difference map (Figure 9c) shows no evident correlation with surface slope. Profile Y-Y' reveals a vertical displacement of  $\sim 1.5$  m across the Pescadores fault from the corrected elevation difference map (Figure 9e), which cannot be seen in the biased height changes (Figure 9d). We estimated an average vertical displacement of 1.2 m over the epicentral area from the corrected elevation difference (Figure 10a). Thus, in order to reliably determine height changes in earthquakes using pre-earthquake and post-earthquake DEMs, horizontal displacement needs to be estimated



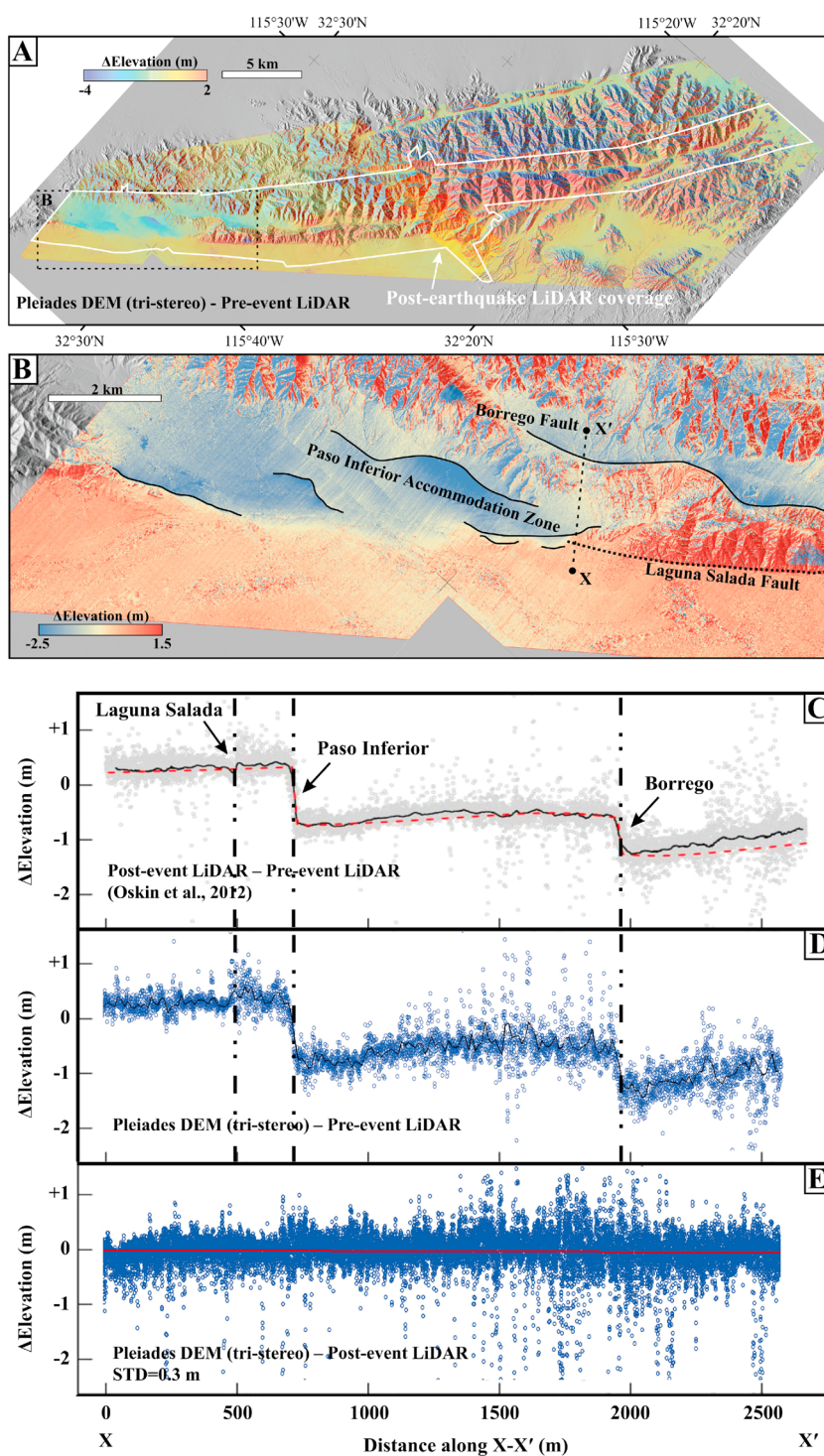


**Figure 8.** (a) Elevation difference map derived from differencing the Pleiades tristereo and pre-earthquake lidar DEMs without accounting for the horizontal displacement. With large topographic relief, elevation difference is strongly affected by surface slope due to the large right-lateral surface slip. Our Pleiades imagery covers a wider area than the post-earthquake lidar DEM (the latter indicated by the white polygon). (b) The elevation differences estimated in this study show distributed deformation in the Paso Inferior accommodation zone (indicated by the box in Figure 8a). (c) Swath profile of elevation difference along line X-X' from Oskin et al. [2012] obtained by differencing the two lidar DEMs. (d) Swath profile of elevation difference along line X-X' of this study by differencing the Pleiades tristereo and pre-earthquake lidar DEMs. The elevation difference map shows meter and submeter offsets along the faults, comparable to the result by differencing the two lidar DEMs. (e) Elevation difference of the Pleiades and post-earthquake lidar DEMs. Outliers result from noise and vegetation.

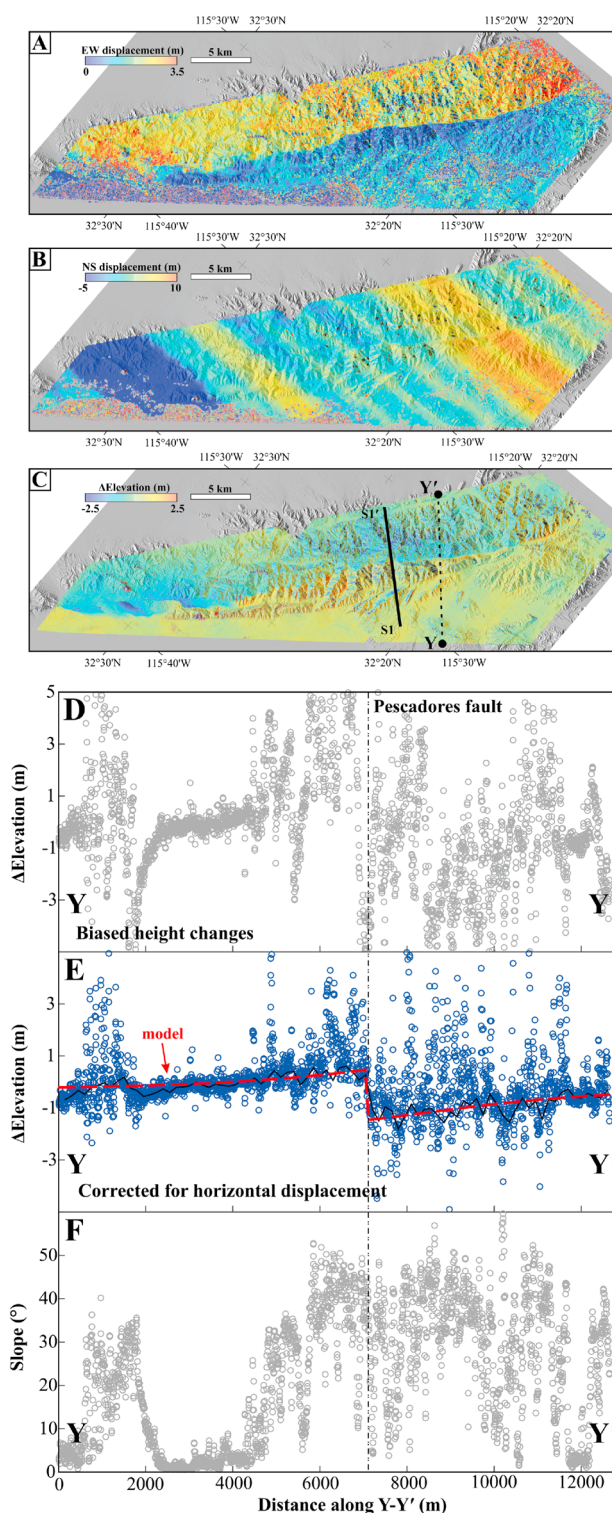


**Figure 9.** (a) East-west component of the horizontal displacement derived from the Pleiades tristereo and pre-earthquake lidar DEMs. (b) North-south component of the horizontal displacement. Note striping artifacts due to laser beam misalignment of the pre-earthquake lidar. (c) Elevation difference map after correcting for the horizontal displacement. S1-S1' is the swath profile in Figure 10. (d) Profile of elevation difference along line Y-Y' from the biased measurements of height changes. (e) Profile of elevation difference along line Y-Y' after correcting for the horizontal displacement (blue circles). Red dashed line shows the elastic dislocation model. (f) Surface slope along line Y-Y'. In flat areas (with surface slopes of less than 5°), the biased height changes agree well with those after correcting for the horizontal displacement; with steep slopes, the influence of the horizontal displacement is significant.



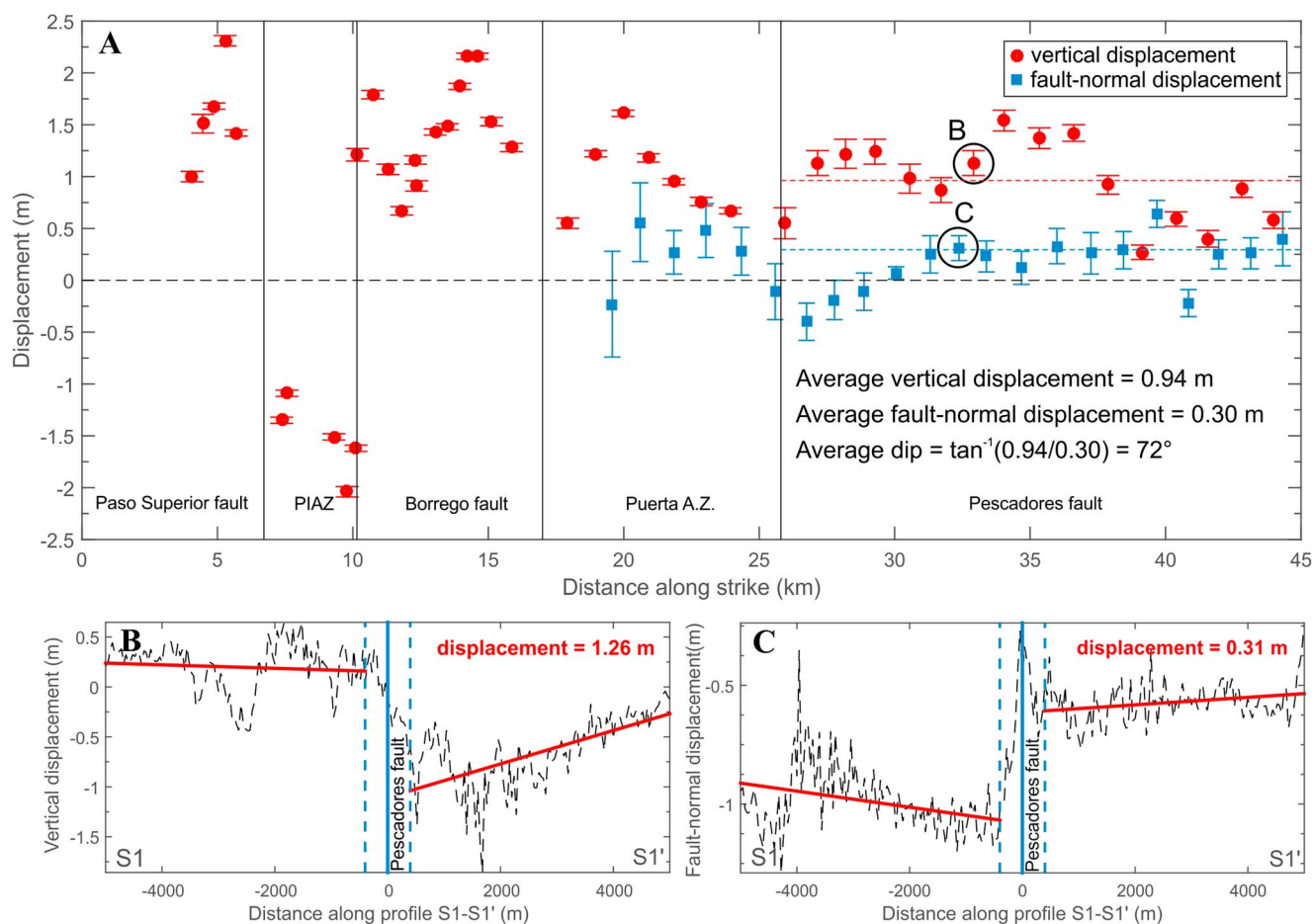


**Figure 10.** (a) Vertical (red dots, positive for southside-up) and fault-normal (blue squares, positive for extension) displacements along the 2010 rupture. PIAZ: Paso Inferior Accommodation Zone. Puerta A.Z.: Puerta Accommodation Zone. The average vertical displacement along the Pescadores fault is 0.94 m (red dashed line), and the average fault-normal displacement is 0.30 m (blue dashed line), from which we estimate an average fault dip of  $72^\circ$ . Circles indicate the locations of Figures 10b and 10c. (b) Swath profile (swath width is 1 km) S1-S1' showing a vertical displacement of 1.26 m (see Figure 9 for location). Blue line denotes the Pescadores fault. Black lines are the measurements. Red lines are the best fitting lines to the measurements on both sides of the fault. We excluded the measurements in the near-fault zone (bounded by blue dashed lines). (c) Swath profile S1-S1' showing a fault-normal displacement of 0.31 m.

and removed first. Whereas *Oskin et al.* [2012] compared their lidar measurements with an elastic model over the Paso Inferior Accommodation Zone, here we focus on the Pescadores fault where topographic slopes are larger than  $30^\circ$ . We reproduced the vertical displacements across the Pescadores fault using a three-dimensional elastic model for a rectangular dislocation [Okada, 1985] with oblique-normal fault slip of 4 m on a fault plane with a strike, dip, and rake of  $312^\circ/75^\circ/-150^\circ$  [Wei et al., 2011] (equivalent to a dip slip of 2 m with a throw of 1.9 m), a length of 100 km, top/bottom depths of 0.001/6 km, and Lamé parameters ( $\lambda = \mu$ ) of  $3.23 \times 10^{10}$  Pa. As shown in Figure 9e, the elastic model agrees well with the height changes determined from the Pleiades and pre-earthquake lidar DEMs.

### 5.3. Estimation of Fault Dip

The detailed 3-D near-field deformation enables us to estimate fault dip ( $\delta$ ) along the rupture using equation (5)

$$\delta = \tan^{-1} \frac{V}{N} \quad (5)$$

where  $V$  and  $N$  are vertical and fault-normal offsets, i.e., throw and heave at the fault.

The vertical and fault-normal offsets in the 2010 earthquake can be obtained from differencing and cross-correlating the pre-earthquake and post-earthquake DEMs (Figure 9). However, as the DEM-derived

displacement in the north-south direction was contaminated by the large systematic deviations in the pre-earthquake lidar DEM (as shown in Figure 9b), here we used the horizontal displacement field from *Barišin et al.* [2015]. Swath profiles (1 km wide) were taken to calculate the dip along the Pescadores fault where the surface rupture is linear. We resolved the east-west and north-south components of the surface displacement onto the fault-normal direction and calculated the fault-normal and vertical offsets by fitting lines on both sides of the fault (see Figure 10). Applying equation (5), the dip was estimated to be  $76^\circ$  for profile S1-S1' (Figures 10b and 10c) with an average of  $72^\circ$  for the Pescadores fault (Figure 10a).

Our estimates of fault dip agree very well with both the field measurements by *Teran et al.* [2015] and the modeling result ( $75^\circ$ ) from seismological and remote sensing observations by *Wei et al.* [2011]. The consistent results suggest that accurate measurements of 3-D near-field deformation provides an additional means of constraining fault geometry.

The El Mayor-Cucapah earthquake has been well studied using remote sensing, seismology, lidar, and field observations, so we focused on comparing our result and results from other well-established studies [*Wei et al.*, 2011; *Oskin et al.*, 2012; *Fletcher et al.*, 2014; *Teran et al.*, 2015; *Barišin et al.*, 2015]. In other areas where field or airborne lidar measurements are difficult, our method based on VHR stereo imagery will be essential for investigating fault geometry. For example, we used Pleiades stereo imagery to study the fault zone deformation of the 2013  $M_w$  7.7 Balochistan earthquake and found that the 200 km long north-dipping Hoshab fault in the eastern Makran switches to south-dipping at its southern end, which may act as the endpoint of earthquake ruptures like the 2013 event (Zhou et al., in review).

## 6. Discussion and Conclusions

This study assesses the capability of the new Pleiades satellites to determine height changes in earthquakes. Two Pleiades tristereo pairs covering part of the 2010  $M_w$  7.2 El Mayor-Cucapah epicentral area were acquired and processed to generate 1 m resolution DEMs. Results from four different combinations of incidence angles (B-N, N-F, B-F, and B-N-F) were compared. Tristereo (B-N-F) can improve the point cloud density by 50% compared to bistereo as it makes full use of all three viewing angles, although with additional costs in acquisition and processing. The tristereo DEM, which incorporates more observations, also has slightly smaller uncertainties than bistereo and thus is more robust and reliable for measuring surface height. The wide stereo angle, e.g., the B-F pair ( $\sim 25^\circ$  corresponding to a B/H ratio of 0.44), makes matching difficult and generates a sparse point cloud ( $\leq 0.4$  points/m<sup>2</sup>), which cannot represent rough topography well, resulting in large uncertainties with increasing slopes above  $\sim 30^\circ$ . If we ignore the contamination of misregistration error due to the different coordinate systems of the Pleiades satellites and lidar, the intrinsic vertical accuracy of the Pleiades DEMs is estimated to be  $\sim 0.3$  m.

By differencing the 1 m Pleiades DEM and the pre-earthquake, lower resolution lidar DEM, we have demonstrated that Pleiades stereo imagery has the capability to determine submeter height changes, e.g.,  $\sim 0.2$  m vertical displacement across the Laguna Salada fault; this result is comparable to a previous study that differenced two lidar DEMs [*Oskin et al.*, 2012]. With subpixel matching using the COSI-Corr software package, we can recover the 3-D surface displacements from the Pleiades and pre-earthquake lidar DEMs. By extension, we expect it to be possible to measure submeter vertical offsets occurring in earthquakes using pre-earthquake and post-earthquake VHR stereo imagery (such as Pleiades and WorldView), without the necessity to conduct a costly lidar survey. Tasking of optical stereo imagery can be relatively rapid but is subject to constraints of cloud cover. Also, the advantages over lidar will be lost in areas that are heavily vegetated, mountainous, or mostly featureless desert salt flats.

In this study, 3-D surface displacements were calculated in two steps. In the first step, we used the pre-earthquake and post-earthquake DEMs to resolve the horizontal displacement. In the second step, we removed the horizontal displacement from the post-earthquake Pleiades DEM and differenced the corrected Pleiades and pre-earthquake lidar DEMs. Recently, *Leprince et al.* [2013] developed a new method that uses multitemporal VHR stereo images to extract topography and derive 3-D ground motion simultaneously. Such a method offers extensive future use for measuring earthquake surface deformation in places where pre-earthquake and post-earthquake images are available.

# Acknowledgments

The Pleiades DEM can be downloaded from OpenTopography (<http://www.opentopography.org/>). The pre-earthquake lidar data were collected and made available by INEGI to enable post-earthquake research and corrected by Craig Glennie, University of Houston (<http://dx.doi.org/10.5069/G9S180F8>). The post-earthquake lidar data were gathered by NCALM at the request of Michael Oskin (UC Davis) in collaboration with Alejandro Hinojosa and John Fletcher of CICESE and Ramon Arrowsmith of Arizona State University (<http://dx.doi.org/10.5069/G9TD9V7D>). The authors would like to thank OpenTopography for expediting access to the pre-earthquake and post-earthquake lidar data. This work was supported by the University of Oxford through a PAG scholarship to Yu Zhou and the Natural Environment Research Council through the Looking into the Continents from Space (LiCS) large grant (NE/K011006/1) and the Centre for the Observation and Modelling of Earthquakes, Volcanoes and Tectonics (COMET). We thank Tim Middleton for helpful discussions. We also thank Mike Poland and two anonymous reviewers for useful comments.

# References

- Avouac, J.-P., and G. Peltzer (1993), Active tectonics in southern Xinjiang, China: Analysis of terrace riser and normal fault scarp degradation along the Hatan-Qira Fault System, *J. Geophys. Res.*, *98*(B12), 21,773–21,807.
- Avouac, J.-P., F. Ayoub, S. Leprince, O. Konca, and D. V. Helmberger (2006), The 2005,  $M_w$  7.6 Kashmir earthquake: Sub-pixel correlation of ASTER images and seismic waveforms analysis, *Earth Planet. Sci. Lett.*, *249*(3), 514–528.
- Avouac, J.-P., F. Ayoub, S. Wei, J.-P. Ampuero, L. Meng, S. Leprince, R. Jolivet, Z. Duputel, and D. Helmberger (2014), The 2013,  $M_w$  7.7 Balochistan earthquake, energetic strike-slip reactivation of a thrust fault, *Earth Planet. Sci. Lett.*, *391*, 128–134.
- Ayoub, F., S. Leprince, and L. Keene (2009), *Users Guide to COSI-CORR Co-Registration of Optically Sensed Images and Correlation*, 38 pp., Calif. Inst. of Technol., Pasadena, Calif.
- Barišin, I., A. Hinojosa-Corona, and B. Parsons (2015), Co-seismic vertical displacements from a single post-seismic lidar DEM: Example from the 2010 El Mayor-Cucapah earthquake, *Geophys. J. Int.*, *202*(1), 328–346.
- Barnhart, W. D., M. J. Willis, R. B. Lohman, and A. K. Melkonian (2011), Insar and optical constraints on fault slip during the 2010–2011 New Zealand earthquake sequence, *Seismol. Res. Lett.*, *82*(6), 815–823.
- Bennett, R. A., W. Rodi, and R. E. Reilinger (1996), Global Positioning System constraints on fault slip rates in southern California and northern Baja, Mexico, *J. Geophys. Res.*, *101*(B10), 21,943–21,960.
- Bernard, M., D. Decluseau, L. Gabet, and P. Nonin (2012), 3D capabilities of Pleiades satellite, *ISPRS International Archives of the Photogrammetry, Remote Sensing and Spatial Information Sciences*, *39*, 553–557.
- Berthier, E., et al. (2014), Glacier topography and elevation changes derived from Pleiades sub-meter stereo images, *Cryosphere*, *8*(6), 2275–2291.
- Besl, P. J., and N. D. McKay (1992), Method for registration of 3-D shapes, in *Robotics-DL Tentative*, pp. 586–606, Int. Soc. for Opt. and Photonics.
- Binet, R., and L. Bollinger (2005), Horizontal coseismic deformation of the 2003 Bam (Iran) earthquake measured from SPOT-5 THR satellite imagery, *Geophys. Res. Lett.*, *32*, L02307, doi:10.1029/2004GL021897.
- Campbell, G., R. Walker, K. Abdrakhmatov, J. Jackson, J. Elliott, D. Mackenzie, T. Middleton, and J.-L. Schwenninger (2015), Great earthquakes in low-strain-rate continental interiors: An example from SE Kazakhstan, *J. Geophys. Res.*, *120*, 5507–5534, doi:10.1002/2015JB011925.
- Cowgill, E. (2007), Impact of riser reconstructions on estimation of secular variation in rates of strike-slip faulting: Revisiting the Charchen river site along the Altyn Tagh Fault, NW China, *Earth Planet. Sci. Lett.*, *254*(3), 239–255.
- de Lussy, F., P. Kubik, D. Greslou, V. Pascal, P. Gigord, and J. P. Cantou (2005), PLEIADES-HR image system products and quality-PLEIADES-HR image system products and geometric accuracy, in *Proceedings of the International Society for Photogrammetry and Remote Sensing Workshop*, Hannover, Germany, 17–20 May.
- de Lussy, F., P. Gigord, and S. Airault (2006), The Pleiades-HR mosaic system product, in *ISPRS International Archives of the Photogrammetry, Remote Sensing and Spatial Information Sciences*, Paris, 4–6 May.
- de Lussy, F., D. Greslou, C. Dechoz, V. Amberg, J. M. Delvit, L. Lebegue, G. Blanchet, and S. Fourest (2012), Pleiades HR in flight geometrical calibration: Location and mapping of the focal plane, *ISPRS International Archives of the Photogrammetry, Remote Sensing and Spatial Information Sciences*, *39*, 519–523.
- Dominguez, S., J.-P. Avouac, and R. Michel (2003), Horizontal coseismic deformation of the 1999 Chi-Chi earthquake measured from SPOT satellite images: Implications for the seismic cycle along the western foothills of central Taiwan, *J. Geophys. Res.*, *108*(B2), 2083, doi:10.1029/2001JB000951.
- Elliott, J., E. Nissen, P. England, J. A. Jackson, S. Lamb, Z. Li, M. Oehlers, and B. Parsons (2012), *Slip in the 2010–2011 Canterbury earthquakes*, *New Zealand*, B03401, vol. 117.
- England, P., and J. Jackson (2011), Uncharted seismic risk, *Nat. Geosci.*, *4*(6), 348–349.
- Fialko, Y., M. Simons, and D. Agnew (2001), The complete (3-D) surface displacement field in the epicentral area of the 1999  $M_w$  7.1 Hector Mine Earthquake, California, from space geodetic observations, *Geophys. Res. Lett.*, *28*(16), 3063–3066.
- Fletcher, J. M., et al. (2014), Assembly of a large earthquake from a complex fault system: Surface rupture kinematics of the 4 April 2010 El Mayor-Cucapah (Mexico)  $M_w$  7.2 earthquake, *Geosphere*, *10*(4), 797–827.
- Fraser, C. S., and H. B. Hanley (2005), Bias-compensated RPCs for sensor orientation of high-resolution satellite imagery, *Photogrammetric Eng. Remote Sens.*, *71*(8), 909–915.
- Fraser, C. S., and M. Ravanbakhsh (2009), Georeferencing accuracy of GeoEye-1 imagery, *Photogrammetric Eng. Remote Sens.*, *75*(6), 634–638.
- Glennie, C. L., A. Hinojosa-Corona, E. Nissen, A. Kusari, M. E. Oskin, J. R. Arrowsmith, and A. Borsa (2014), Optimization of legacy lidar data sets for measuring near-field earthquake displacements, *Geophys. Res. Lett.*, *41*, 3494–3501, doi:10.1002/2014GL059919.
- Gold, R. D., and E. Cowgill (2011), Deriving fault-slip histories to test for secular variation in slip, with examples from the Kunlun and Awatere faults, *Earth Planet. Sci. Lett.*, *301*(1), 52–64.
- Gremban, K. D., C. E. Thorpe, and T. Kanade (1988), Geometric camera calibration using systems of linear equations, in *International Conference on Robotics and Automation*, vol. 1, pp. 562–567, IEEE, Philadelphia, P. A.
- Grodecki, J., and G. Dial (2003), Block adjustment of high-resolution satellite images described by rational polynomials, *Photogrammetric Eng. Remote Sens.*, *69*(1), 59–68.
- Hanks, T. C., R. C. Bucknam, K. R. Lajoie, and R. E. Wallace (1984), Modification of wave-cut and faulting-controlled landforms, *J. Geophys. Res.*, *89*(B7), 5771–5790.
- Hauksson, E., J. Stock, K. Hutton, W. Yang, J. A. Vidal-Villegas, and H. Kanamori (2011), The 2010  $M_w$  7.2 El Mayor-Cucapah Earthquake Sequence, Baja California, Mexico and Southernmost California, USA: Active seismotectonics along the Mexican Pacific Margin, *Pure Appl. Geophys.*, *168*(8–9), 1255–1277.
- Hollingsworth, J., S. Leprince, F. Ayoub, and J.-P. Avouac (2012), Deformation during the 1975–1984 Krafla rifting crisis, NE Iceland, measured from historical optical imagery, *J. Geophys. Res.*, *117*, B11407, doi:10.1029/2012JB009140.
- Hu, Y., V. Tao, and A. Croitoru (2004), Understanding the rational function model: Methods and applications, *Int. Arch. Photogramm. Remote Sens.*, *20*(6), 663–668.
- Jackson, J. (2001), Living with earthquakes: Know your faults, *J. Earthquake Eng.*, *5*, 5–123.
- Klinger, Y., X. Xu, P. Tapponnier, J. Van der Woerd, C. Lasserre, and G. King (2005), High-resolution satellite imagery mapping of the surface rupture and slip distribution of the  $M_w$  7.8, 14 November 2001 Kokoxili earthquake, Kunlun fault, northern Tibet, China, *Bull. Seismol. Soc. Am.*, *95*(5), 1970–1987.
- Leprince, S., S. Barbot, F. Ayoub, and J.-P. Avouac (2007), Automatic and precise orthorectification, coregistration, and subpixel correlation of satellite images, application to ground deformation measurements, *IEEE Trans. Geosci. Remote Sens.*, *45*(6), 1529–1558.

- Leprince, S., J. Lin, F. Ayoub, F. Herman, and J. Avouac (2013), *3D High Resolution Tracking of Ice Flow Using Mutli-Temporal Stereo Satellite Imagery, Franz Josef Glacier, New Zealand*, AGU Fall Meeting, San Francisco, Calif., 9–13 Dec.
- Michel, R., and J.-P. Avouac (2002), Deformation due to the 17 August 1999 Izmit, Turkey, earthquake measured from SPOT images, *J. Geophys. Res.*, *107*(B4), 2062, doi:10.1029/2000JB000102.
- Mitchell, G., and K. MacNabb (2010), High resolution stereo satellite elevation mapping accuracy assessment, *ASPRS Annual Conference*, ASPRS, San Diego, Calif., 26–30 Apr.
- Molnar, P., and P. Tapponnier (1975), Cenozoic tectonics of Asia: Effects of a continental collision, *Science*, *189*(4201), 419–426.
- Nissen, E., A. K. Krishnan, J. R. Arrowsmith, and S. Saripalli (2012), *Three-Dimensional Surface Displacements and Rotations From Differencing Pre- and Post-Earthquake LiDAR Point Clouds*, L16301, vol. 39.
- Nissen, E., T. Maruyama, J. R. Arrowsmith, J. R. Elliott, A. K. Krishnan, M. E. Oskin, and S. Saripalli (2014), Coseismic fault zone deformation revealed with differential lidar: Examples from Japanese  $M_w \sim 7$  intraplate earthquakes, *Earth Planet. Sci. Lett.*, *405*, 244–256, doi:10.1016/j.epsl.2014.08.031.
- Oh, J., and C. Lee (2014), Automated bias-compensation of rational polynomial coefficients of high resolution satellite imagery based on topographic maps, *ISPRS J. Photogramm. Remote Sens.*, *100*, 12–22.
- Okada, Y. (1985), Surface deformation due to shear and tensile faults in a half-space, *Bull. Seismol. Soc. Am.*, *75*(4), 1135–1154.
- Oskin, M. E., K. Le, and M. D. Strane (2007), Quantifying fault-zone activity in arid environments with high-resolution topography, *Geophys. Res. Lett.*, L23505, doi:10.1029/2007GL031295.
- Oskin, M. E., J. R. Arrowsmith, A. H. Corona, A. J. Elliott, J. M. Fletcher, E. J. Fielding, P. O. Gold, J. J. G. Garcia, K. W. Hudnut, J. Liu-Zeng, and O. J. Teran (2012), Near-field deformation from the El Mayor-Cucapah earthquake revealed by differential LIDAR, *Science*, *335*(6069), 702–705.
- Poli, D., and T. Toutin (2012), Review of developments in geometric modelling for high resolution satellite pushbroom sensors, *Photogramm. Record*, *27*(137), 58–73.
- Ren, Z., Z. Zhang, T. Chen, S. Yan, J. Yin, P. Zhang, W. Zheng, H. Zhang, and C. Li (2015), Clustering of offsets on the Haiyuan fault and their relationship to paleoearthquakes, *Geol. Soc. Am. Bull.*, *B31*, B31155.
- Ritz, J., E. Brown, D. Bourles, H. Philip, A. Schlupp, G. Raisbeck, F. Yiou, and B. Enkhuvshin (1995), Slip rates along active faults estimated with cosmic-ray — Exposure dates: Application to the Bogd fault, Gobi-Altaï, Mongolia, *Geology*, *23*(11), 1019–1022.
- Smith, W., and P. Wessel (1990), Gridding with continuous curvature splines in tension, *Geophysics*, *55*(3), 293–305.
- Stumpf, A., J.-P. Malet, P. Allemand, and P. Ulrich (2014), Surface reconstruction and landslide displacement measurements with Pléiades satellite images, *ISPRS J. Photogramm. Remote Sens.*, *95*, 1–12.
- Teran, O. J., J. M. Fletcher, M. E. Oskin, T. K. Rockwell, K. W. Hudnut, R. M. Spelz, S. O. Akciz, A. P. Hernandez-Flores, and A. E. Morelan (2015), Geologic and structural controls on rupture zone fabric: A field-based study of the 2010  $M_w$  7.2 El Mayor-Cucapah earthquake surface rupture, *Geosphere*, *11*(3), 899–920.
- Wallace, R. E. (1977), Profiles and ages of young fault scarps, north-central Nevada, *Geol. Soc. Am. Bull.*, *88*(9), 1267–1281.
- Wei, S., et al. (2011), Superficial simplicity of the 2010 El Mayor-Cucapah earthquake of Baja California in Mexico, *Nat. Geosci.*, *4*(9), 615–618.
- Wesnousky, S. G., S. Kumar, R. Mohindra, and V. Thakur (1999), Uplift and convergence along the Himalayan Frontal Thrust of India, *Tectonics*, *18*(6), 967–976.
- Zhang, P.-Z. (2013), Beware of slowly slipping faults, *Nat. Geosci.*, *6*(5), 323–324.
- Zhou, Y., J. R. Elliott, B. Parsons, and R. T. Walker (2015), The 2013 Balochistan earthquake: An extraordinary or completely ordinary event?, *Geophys. Res. Lett.*, *42*(15), 6236–6243, doi:10.1002/2015GL065096.